論文 / 著書情報
Article / Book Information

Title	Source-position-dependent transmission cross coefficient formula including polarization and mask three-dimensional effects in high-numerical-aperture extreme ultraviolet lithography
Authors	Hiroyoshi Tanabe, Moe Sugiyama, Masayuki Shimoda, Atsushi Takahashi
Citation	Journal of Micro/Nanopatterning, Materials and Metrology (JM3)
Pub. date	2026, 5
DOI	https://doi.org/10.1117/1.JMM.25.3.031604
Rights	(Copyright) CC BY: (c) The Authors. Published by SPIE under a Creative Commons Attribution 4.0 International License (See next page.).Distribution or reproduction of this work in whole or in part requires full attribution of the original publication, including its DOI. [https://doi.org/10.1117/1.JMM.25.3.031604] (Citation) Hiroyoshi Tanabe, Moe Sugiyama, Masayuki Shimoda, and Atsushi Takahashi "Source-position-dependent transmission cross coefficient formula including polarization and mask three-dimensional effects in high-numerical-aperture extreme ultraviolet lithography," Journal of Micro/Nanopatterning, Materials, and Metrology 25(3), 031604 (4 May 2026). https://doi.org/10.1117/1.JMM.25.3.031604

JM3 Journal of Micro/Nanopatterning, Materials, and Metrology

RESEARCH PAPER

Source-position-dependent transmission cross coefficient formula including polarization and mask three-dimensional effects in high-numerical-aperture extreme ultraviolet lithography

Hiroyoshi Tanabe,* Moe Sugiyama, Masayuki Shimoda, and Atsushi Takahashi
Institute of Science Tokyo, Meguro-ku, Japan

ABSTRACT. Background: Hopkins' transmission cross coefficient (TCC) formula is conventionally used in optical lithography simulations. In extreme ultraviolet (EUV) lithography, the TCC formula must be modified to account for the mask 3D (M3D) effect of the thick EUV mask absorber. In the previous paper, we proposed the source-position-dependent TCC (STCC) formula, which used three TCCs (TCC, TCCSX, and TCCSY) to represent the source-position dependence of the M3D effect.

Aim: The polarization effect is not negligible in high-NA EUV lithography. The purpose of this work is to extend the STCC formula to include the polarization effect and enable accurate and fast simulation of polarization-dependent imaging in high-NA EUV lithography.

Approach: To include the polarization effect, an additional coherence function C_ρ must be introduced into the STCC formula. C_ρ represents the effect of the electric field rotation in the meridional plane, which depends on the polarization $\rho = x$ or y.

Results: Six TCCs (TCC_ρ, TCCSX_ρ, and TCCSY_ρ) are required to include both the polarization and M3D effects in the STCC formula. For mask patterns with vertical lines, 18 TCCs are required.

Conclusions: The STCC formula is extended for high-NA EUV lithography simulations. The STCC formula is the basis of our convolutional neural network model, which accelerates EUV lithography simulations.

[DOI: 10.1117/1.JMM.25.3.031604]

Keywords: lithography simulation; neural network; EUV mask

Paper 25109SS received Oct. 23, 2025; revised Mar. 19, 2026; accepted Apr. 8, 2026; published May 4, 2026.

1 Introduction

The thin mask model has been used in optical lithography simulations. In this model, the far-field diffraction amplitudes from a thin optical mask are calculated by a Fourier transform of the mask pattern. However, in extreme ultraviolet (EUV) lithography, the thin mask model is not valid because the absorber thickness is comparable to the mask pattern size. High-aspect absorbers induce several mask 3D (M3D) effects, such as contrast fading, best focus shifts, and nontelecentricity, which result in the critical dimension (CD) error and edge placement error.[1,2] M3D effects are caused by the distorted diffraction amplitude from a thick EUV mask (Fig. 1). Both the near-field and far-field diffraction amplitudes can be calculated rigorously using electromagnetic

---

*Address all correspondence to Hiroyoshi Tanabe, tanabe@eda.ict.eng.isct.ac.jp

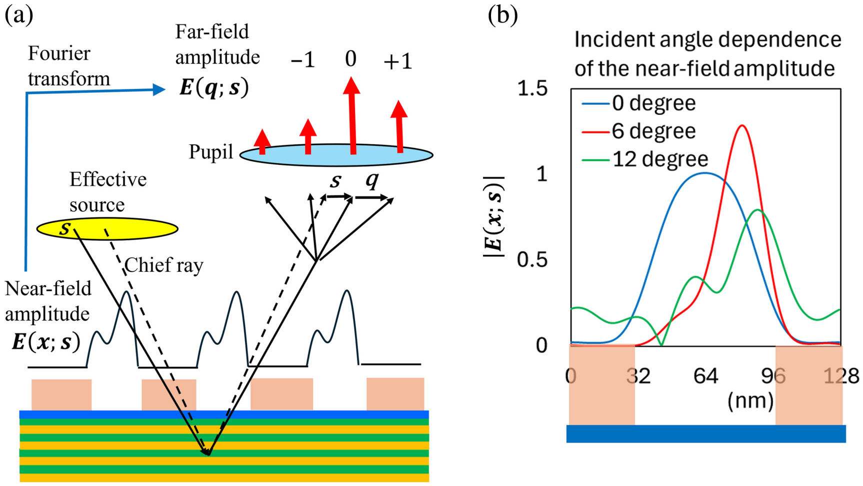

Fig. 1 (a) Near-field and far-field diffraction amplitudes from an EUV mask. (b) Incident angle dependence of the near-field amplitude.

(EM) simulators.[3–5] These calculations are highly time-consuming and not suited for optical proximity correction (OPC) applications.

In optical lithography simulations, the sum of coherent systems (SOCS) model[6] is often employed for OPC applications to accelerate the computation. The SOCS model decomposes Hopkins' transmission cross coefficient[7,8] (TCC) into a set of eigenvalues and eigenvectors. The TCC formula is equivalent to Abbe's theory,[9] assuming the thin mask model. In this model, the far-field diffraction amplitude is the Fourier transform of the mask pattern $M^{\mathrm{FT}}(\boldsymbol{q})$, which is a function of the diffraction momentum (or wave vector) $\boldsymbol{q}$. The diffraction momentum has a discrete value (diffraction order) assuming a periodic mask pattern. The diffraction amplitude of the thin mask model, $M^{\mathrm{FT}}(\boldsymbol{q})$ does not depend on the source position (or incident angle) $\boldsymbol{s}$. However, as shown in Fig. 1, the far-field diffraction amplitude from an EUV mask (thick mask), $\boldsymbol{E}(\boldsymbol{q};\boldsymbol{s})$ depends on both $\boldsymbol{q}$ and $\boldsymbol{s}$. Therefore, the TCC formula cannot be used for EUV lithography simulations, as explained in Sec. 2.

In our previous paper,[10] the source position dependence of the diffraction amplitude from an EUV mask was approximated as a linear function of the incident momentum. We defined the coefficients of the linear function as M3D parameters. By inserting the linear approximation of the diffraction amplitude into Abbe's theory, the source-position-dependent TCC (STCC) formula was derived, which contained three different TCCs. The SOCS model was applied to each TCC to accelerate the computation.

M3D parameters are uniquely calculated from the mask pattern. A convolutional neural network (CNN) was constructed that predicts M3D parameters from an input mask pattern. The CNN prediction was 2400 times faster than the EM simulation.[11]

In the previous paper, we assumed that the NA of EUV optics was 0.33. Recently, high-NA (NA 0.55) EUV scanners have been installed at several sites.[12] The polarization effect is large in high-NA optics, and several models[13,14] were proposed to include the polarization effect in the lithography simulation. In these models, Abbe's theory was implicitly used to calculate image intensity. However, there was no explanation of how to convert Abbe's theory into the TCC formula in the presence of polarization. In this work, the STCC formula is extended to include the polarization effect.

In Sec. 2, we review the STCC formula that includes M3D effects. In Sec. 3, the STCC formula is extended to include the polarization effect, which is not negligible in high-NA EUV lithography. In Sec. 4, the accuracy of the STCC formula is verified. In Sec. 5, the CNN model for fast EUV lithography simulation is explained. Section 6 is the summary.

2 STCC Formula Including the M3D Effects

This section is the review of the STCC formula in Ref. 10.

In optical lithography, the image intensity $I(\boldsymbol{x})$ on a wafer is calculated using Abbe's theory as follows.

$$I(\boldsymbol{x}) = \iint S(\boldsymbol{s}) \left| \iint M^{\mathrm{FT}}(\boldsymbol{q}) P(\boldsymbol{q}+\boldsymbol{s}) e^{i(M_x q_x + M_y q_y y)} \mathrm{d}\boldsymbol{q} \right|^2 \mathrm{d}\boldsymbol{s}, \tag{1}$$

where S and P represent the effective source and the pupil function of the projection optics. M_x and M_y are the magnifications of the mask in the x and y directions. The Fourier transform of the mask pattern $M^{\mathrm{FT}}(\boldsymbol{q})$ is a function of the diffraction momentum $\boldsymbol{q} = (q_x, q_y, 0)$, but it does not depend on the source position $\boldsymbol{s} = (s_x, s_y, 0)$.

In Refs. 7 and 8, Hopkins' TCC formula is derived from the mutual coherence theory, assuming the thin mask model (i.e., the transmittance of the object does not depend on the incident angle). This formula can also be derived by changing the order of the integrations in Eq. (1) as follows,

$$I(\boldsymbol{x}) = \iint TCC(\boldsymbol{q};\boldsymbol{q}') M^{\mathrm{FT}}(\boldsymbol{q}) M^{\mathrm{FT}*}(\boldsymbol{q}') e^{iM_x(q_x - q_x')x + iM_y(q_y - q_y')y} \mathrm{d}\boldsymbol{q}\, \mathrm{d}\boldsymbol{q}', \tag{2}$$

$$TCC(\boldsymbol{q};\boldsymbol{q}') = \iint S(\boldsymbol{s}) P(\boldsymbol{q}+\boldsymbol{s}) P^*(\boldsymbol{q}'+\boldsymbol{s}) \mathrm{d}\boldsymbol{s}. \tag{3}$$

The TCC does not depend on the mask pattern M. Therefore, the TCC is precomputed and stored in memory to speed up the image intensity calculation.

The computation of the image intensity is further accelerated using the SOCS model.[6] The SOCS model decomposes the TCC into a set of eigenvalues λ_m and eigenvectors ϕ_m as follows:

$$TCC(\boldsymbol{q};\boldsymbol{q}') = \sum_m \lambda_m \phi_m(\boldsymbol{q}) \phi_m^*(\boldsymbol{q}'). \tag{4}$$

Then, the image intensity is calculated by the following equation,

$$I(\boldsymbol{x}) = \sum_m \lambda_m \left| \iint \phi_m(\boldsymbol{q}) M^{\mathrm{FT}}(\boldsymbol{q}) e^{i(M_x q_x x + M_y q_y y)} \mathrm{d}\boldsymbol{q} \right|^2. \tag{5}$$

The computation of the SOCS model becomes extremely fast by selecting large eigenvalues, which gives dominant contributions to the image intensity.

In EUV lithography, Abbe's theory is also valid to calculate the image intensity. The Fourier transform of the mask pattern $M^{\mathrm{FT}}(\boldsymbol{q})$ in Eq. (1) is replaced by the far-field electric amplitude $\boldsymbol{E}(\boldsymbol{q};\boldsymbol{s})$ as follows:

$$I(\boldsymbol{x}) = \iint S(\boldsymbol{s}) \left| \iint \boldsymbol{E}(\boldsymbol{q};\boldsymbol{s}) P(\boldsymbol{q}+\boldsymbol{s}) e^{i(M_x q_x x + M_y q_y y)} \mathrm{d}\boldsymbol{q} \right|^2 \mathrm{d}\boldsymbol{s}. \tag{6}$$

As the far-field electric amplitude $\boldsymbol{E}(\boldsymbol{q};\boldsymbol{s})$ depends on the source position $\boldsymbol{s}$, the order of the integration in Eq. (6) cannot be changed. Therefore, Hopkins' TCC formula cannot be applied to EUV lithography simulations.

The far-field electric amplitude $\boldsymbol{E}(\boldsymbol{q};\boldsymbol{s})$ is a continuous function of the source position $\boldsymbol{s}$ as shown in Fig. 2. To change the order of the integrations in Eq. (6), we approximate the electric field $\boldsymbol{E}(\boldsymbol{q};\boldsymbol{s})$ as a linear function of the source position $\boldsymbol{s}$ as follows,

$$\boldsymbol{E}(\boldsymbol{q};\boldsymbol{s}) \cong \boldsymbol{E}(\boldsymbol{q}) + \partial_{s_x}\boldsymbol{E}(\boldsymbol{q})(s_x + q_x/2) + \partial_{s_y}\boldsymbol{E}(\boldsymbol{q})(s_y + q_y/2), \tag{7}$$

where

$$\boldsymbol{E}(\boldsymbol{q}) = \boldsymbol{E}(\boldsymbol{q};\boldsymbol{s} = -\boldsymbol{q}/2), \tag{8}$$

$$\partial_{s_x}\boldsymbol{E}(\boldsymbol{q}) = \left.\frac{\partial \boldsymbol{E}(\boldsymbol{q};\boldsymbol{s})}{\partial s_x}\right|_{\boldsymbol{s}=-\boldsymbol{q}/2}, \tag{9}$$

$$\partial_{s_y}\boldsymbol{E}(\boldsymbol{q}) = \left.\frac{\partial \boldsymbol{E}(\boldsymbol{q};\boldsymbol{s})}{\partial s_y}\right|_{\boldsymbol{s}=-\boldsymbol{q}/2}. \tag{10}$$

The origin of the linear expansion in Eq. (7) is $\boldsymbol{s} = -\boldsymbol{q}/2$. This position is the center of the overlapping area of the effective source $S(\boldsymbol{s})$ and the pupil $P(\boldsymbol{q}+\boldsymbol{s})$, assuming the effective source

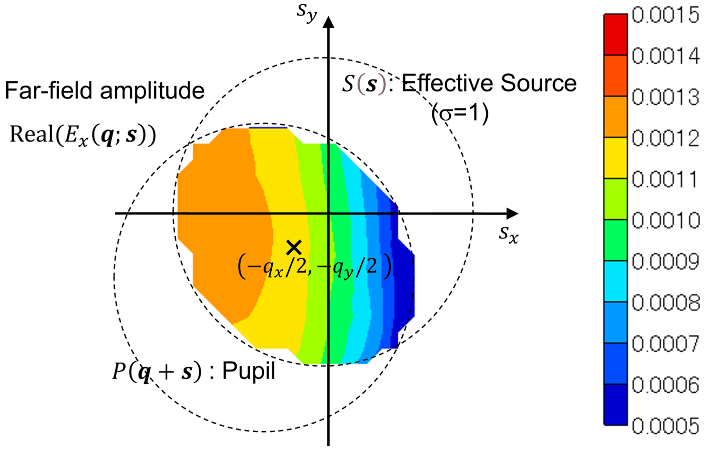

Fig. 2 Far-field amplitude in the overlapping area of the effective source and the pupil.

size $\sigma = 1$ (see Fig. 2). Only the overlapping area contributes to the image intensity integration in Eq. (6).

Inserting Eq. (7) into Eq. (6) we obtain,

$$I(\boldsymbol{x}) \cong \iint S(\boldsymbol{s}) \left| \iint (\boldsymbol{E}(\boldsymbol{q}) + \partial_{s_x}\boldsymbol{E}(\boldsymbol{q})(s_x + q_x/2) + \partial_{s_y}\boldsymbol{E}(\boldsymbol{q})(s_y + q_y/2))P(\boldsymbol{q}+\ \boldsymbol{s}) \times e^{i(M_x q_x x + M_y q_y y)} \mathrm{d}\boldsymbol{q} \right|^2 \mathrm{d}\boldsymbol{s}. \tag{11}$$

By changing the order of the integrations, this equation can be decomposed as follows,

$$\begin{aligned} I(\boldsymbol{x}) \cong & \iint TCC(\boldsymbol{q};\boldsymbol{q}')\boldsymbol{E}(\boldsymbol{q}) \cdot \boldsymbol{E}(\boldsymbol{q}')^* e^{iM_x(q_x-q_x')x + iM_y(q_y-q_y')y} \mathrm{d}\boldsymbol{q}\,\mathrm{d}\boldsymbol{q} \\ & + 2\,\mathrm{Re}\left\{ \iint TCC(\boldsymbol{q};\boldsymbol{q}')\boldsymbol{E}(\boldsymbol{q}) \cdot (\partial_{s_x}\boldsymbol{E}(\boldsymbol{q}')q_x'/2 + \partial_{s_y}\boldsymbol{E}(\boldsymbol{q}')q_y'/2)^* e^{iM_x(q_x-q_x')x + iM_y(q_y-q_y')y} \mathrm{d}\boldsymbol{q}\,\mathrm{d}\boldsymbol{q}' \right\} \\ & + 2\,\mathrm{Re}\left\{ \iint TCCSX(\boldsymbol{q};\boldsymbol{q}')\boldsymbol{E}(\boldsymbol{q}) \cdot \partial_{s_x}\boldsymbol{E}(\boldsymbol{q}')^* e^{iM_x(q_x-q_x')x + iM_y(q_y-q_y')y} \mathrm{d}\boldsymbol{q}\,\mathrm{d}\boldsymbol{q}' \right\} \\ & + 2\,\mathrm{Re}\left\{ \iint TCCSY(\boldsymbol{q};\boldsymbol{q}')\boldsymbol{E}(\boldsymbol{q}) \cdot \partial_{s_y}\boldsymbol{E}(\boldsymbol{q}')^* e^{iM_x(q_x-q_x') + iM_y(q_y-q_y')y} \mathrm{d}\boldsymbol{q}\ \mathrm{d}\boldsymbol{q}' \right\}, \end{aligned} \tag{12}$$

where *TCC*, *TCCSX*, and *TCCSY* are defined by the following equations,

$$TCC(\boldsymbol{q};\boldsymbol{q}') = \iint S(\boldsymbol{s})P(\boldsymbol{q}+\boldsymbol{s})P^*(\boldsymbol{q}'+\boldsymbol{s})\mathrm{d}\boldsymbol{s}, \tag{13}$$

$$TCCSX(\boldsymbol{q};\boldsymbol{q}') = \iint s_x S(\boldsymbol{s})P(\boldsymbol{q}+\boldsymbol{s})P^*(\boldsymbol{q}'+\boldsymbol{s})\mathrm{d}\boldsymbol{s}, \tag{14}$$

$$TCCSY(\boldsymbol{q};\boldsymbol{q}') = \iint s_y S(\boldsymbol{s})P(\boldsymbol{q}+\boldsymbol{s})P^*(\boldsymbol{q}'+\boldsymbol{s})\mathrm{d}\boldsymbol{s}. \tag{15}$$

The quadratic terms of s_x and s_y that appear in the expansion of Eq. (11) are ignored in Eq. (12). We call this formula source-position-dependent TCC (STCC).

To speed up the computation, the SOCS model is applied to the Hermitian matrices *TCC*, *TCCSX*, and *TCCSY*. Then, three TCCs are written as

$$TCC(\boldsymbol{q};\boldsymbol{q}') = \sum_n \alpha_n \varphi_n(\boldsymbol{q})\varphi_n^*(\boldsymbol{q}'), \tag{16}$$

$$TCCSX(\boldsymbol{q};\boldsymbol{q}') = \sum_n \beta_n \phi_n(\boldsymbol{q})\phi_n^*(\boldsymbol{q}'), \tag{17}$$

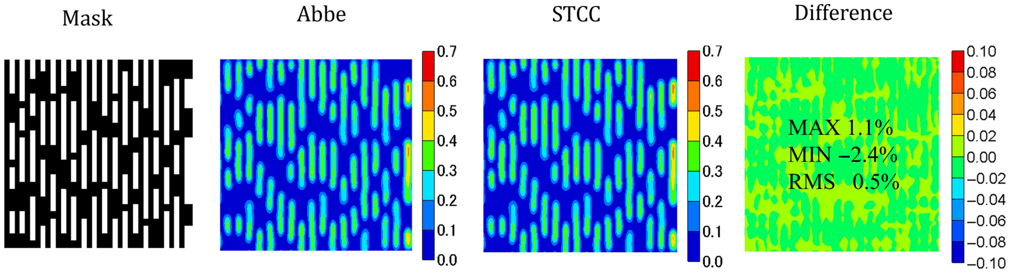

Fig. 3 Image intensities calculated by Abbe's theory and STCC formula.

$$TCCSY(\boldsymbol{q};\boldsymbol{q}') = \sum_n \gamma_n \psi_n(\boldsymbol{q}) \psi_n^*(\boldsymbol{q}'), \tag{18}$$

where $\alpha_n, \beta_n, \gamma_n$ are eigenvalues and $\varphi_n, \phi_n, \psi_n$ are eigenvectors.

Figure 3 compares the image intensities calculated by Abbe's theory and the STCC formula. The far-field electric amplitude $\boldsymbol{E}(\boldsymbol{q};\boldsymbol{s})$ is calculated using the 3D waveguide model in Ref. 11. The mask pattern has 14 nm vertical spaces. The optical setting is NA 0.33, and the dipole illumination is DX90 with $\sigma_{\text{in}}/\sigma_{\text{out}} = 0.55/0.9$. The absorber material is Ta, and the thickness of the absorber is 60 nm. As shown in Fig. 3, the linear approximation of the STCC formula gives good accuracy. The root mean square (RMS) of the difference between the intensities calculated by Abbe's theory and the STCC formula is 0.5%. The intensity difference is normalized by the reflectivity of the multilayer, 0.64.

Linear approximation of the source-position dependence of diffraction amplitudes is the first step to include the M3D effects in TCC formula. However, as shown in Fig. 2, there remain nonlinear terms in the source-position dependence of diffraction amplitudes. The contribution of the nonlinear terms will be discussed in Sec. 4.

To obtain the results of the STCC formula in Fig. 3, the SOCS model was not applied, and Eq. (12) was used straightforwardly. Although detailed investigations have not yet been performed, when the SOCS model was used, good accuracy was obtained using 100 eigenmodes for *TCC* and 20 eigenmodes for *TCCSX* and *TCCSY*.

3 STCC Formula Including the Polarization and M3D Effects

In Sec. 2, we derived the STCC formula including M3D effects. The polarization effect is ignored, assuming the NA of EUV optics is 0.33. However, the polarization effect becomes large in high-NA optics. The rotation of the electric field inside the projection optics causes the degradation of the image contrast on the wafer. As shown in Fig. 4, when the electric field is in the meridional plane, i.e., in the case of transverse magnetic (TM) wave, the image contrast becomes low in high-NA optics.

3.1 Representation of the Polarization by Vector Potential

The Jones vector is often used to represent the polarization of the light. The Jones vector has two electric field components E_x and E_y, and E_z is set to zero, assuming the light is traveling in the z

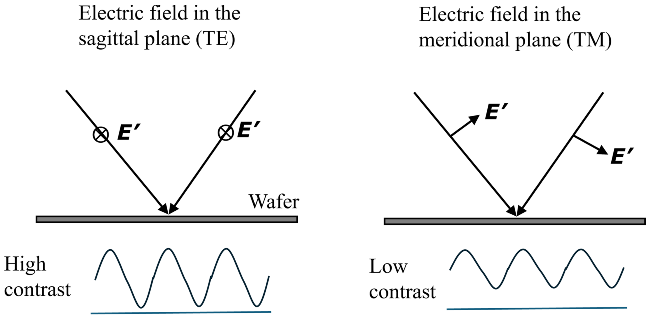

Fig. 4 Image contrast difference between two polarizations.

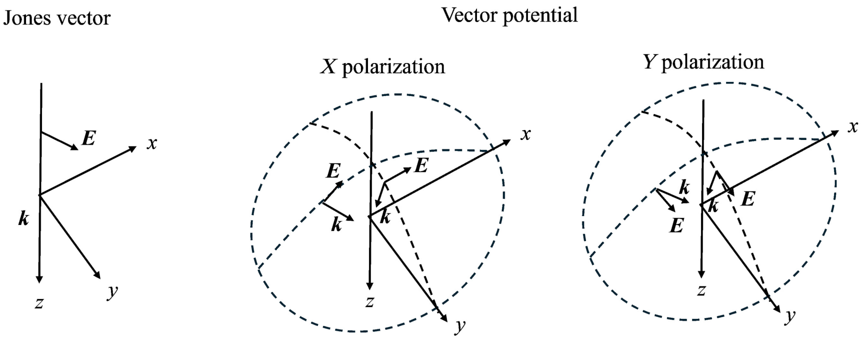

Fig. 5 Representations of polarization by Jones vector and vector potential. In the Jones vector representation, light travels in the z direction. In the vector potential representation, light travels in any direction.

direction. In Ref. 15, we proposed a new representation of polarization using vector potential. The vector-potential representation is a more general representation of polarization than the Jones vector because it does not assume that the light is travelling in the z direction. Figure 5 compares the Jones vector representation and the vector-potential representation.

As shown in Ref. 15, the electric field of light in free space is written by the vector potential $\boldsymbol{A}$ as follows,

$$\boldsymbol{E} = \mathrm{i}k\boldsymbol{A} - \frac{\mathrm{i}}{k}(\boldsymbol{k}\cdot\boldsymbol{A})\boldsymbol{k}, \tag{19}$$

where $\boldsymbol{k}$ is the wavevector and k is the wavenumber. It can be easily proved that the electric field is perpendicular to the wave vector,

$$\boldsymbol{E}\cdot\boldsymbol{k} = 0. \tag{20}$$

The vector-potential representation has two polarizations.

X polarization:

$$\boldsymbol{A} = (A_x, 0, 0), \tag{21}$$

$$\boldsymbol{E} = \frac{\mathrm{i}A_x}{k}(k^2 - k_x^2, -k_y k_x, -k_z k_x). \tag{22}$$

Y polarization:

$$\boldsymbol{A} = (0, A_y, 0), \tag{23}$$

$$\boldsymbol{E} = \frac{\mathrm{i}A_y}{k}(-k_x k_y, k^2 - k_y^2, -k_z k_y). \tag{24}$$

The z component of the vector potential A_z can be fixed to zero by the gauge transformation.[15] The vector-potential representation of polarization has two degrees of freedom.

3.2 Polarization Changes at the EUV Mask

The incoming wave from the effective source is diffracted by the EUV mask. The diffraction changes the polarization of the incoming wave. Even when the incoming wave has X polarization, the outgoing wave has both X and Y polarizations. However, as shown in Ref. 15, the polarization changes at the mask are very small in EUV lithography. This is because the refractive index of the EUV absorber is close to 1. In optical fiber theory, the refractive index of the core is close to that of the cladding, and the weakly guiding approximation[16] is often used, which decouples the two polarizations. This approximation can be applied to EUV lithography.[15] As shown in Fig. 6, the difference between the image intensities calculated by the vector model and the weakly guiding approximation (scalar model) is very small, less than 0.1%. Therefore, in this paper, the polarization changes at the mask are ignored.

In Fig. 7 of Ref. 15 we showed the result of the weakly guiding approximation when the low-n absorber TP1[17] was used. The complex refractive index of the TP1 absorber is (0.91, 0.032).

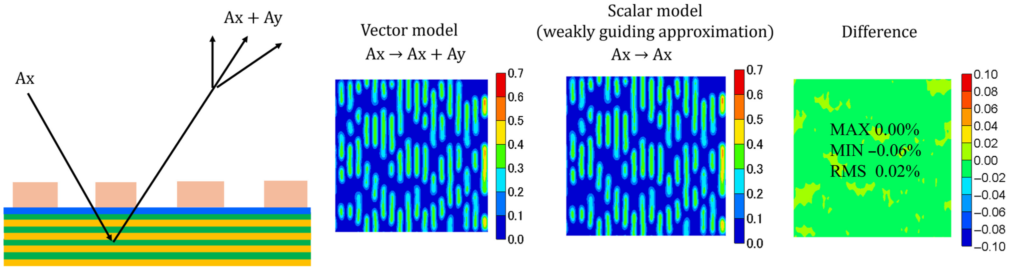

Fig. 6 Polarization changes and the comparison between the vector and scalar models.

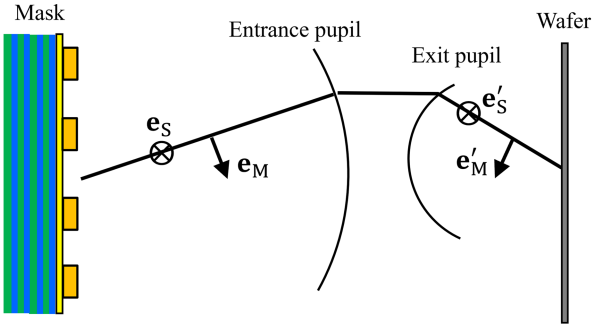

Fig. 7 Rotation of the electric field inside the projection optics in the meridional plane.

The accuracy of the approximation deteriorated when the low-n absorber was used. The low-n absorber is still under development, and the mask process has not yet been established.[17] Development of the low-n absorber mask is still progressing.[18] When the development is completed, the polarization change at the EUV mask will need to be reconsidered.

Note that the weakly guiding approximation could not be used for ArF lithography simulations, where the refractive indices of the membranes are much larger than that of the air.

3.3 Rotation of the Electric Field Inside the Projection Optics

According to Ref. 19, the electric field in the meridional plane rotates inside the projection optics. On the other hand, the direction of the electric field in the sagittal plane does not change, as shown in Fig. 7. In the figure, $\mathbf{e}_M$ ($\mathbf{e}_S$) and $\mathbf{e}'_M$ ($\mathbf{e}'_S$) are the unit vectors in the meridional plane (sagittal plane) at the mask and wafer, respectively.

Figure 8 shows the outgoing wave at the mask and the incoming wave at the wafer. In the figure, $\boldsymbol{s}_0$ is the momentum of the chief ray at the mask defined by

$$\boldsymbol{s}_0 = \left(s_{0x}, s_{0y}, -\sqrt{k^2 - (s_{0x})^2 - (s_{0y})^2}\right), \tag{25}$$

$$s_{0x} = k \sin\theta \sin\varphi, \tag{26}$$

$$s_{0y} = k \sin\theta \cos\varphi, \tag{27}$$

where θ and φ are the incident angle and the azimuthal angle (from the y axis) of the chief ray at the mask, respectively. The outgoing momentum at the mask is $\boldsymbol{p} + \boldsymbol{s}_0$, and $\boldsymbol{p} = \boldsymbol{q} + \boldsymbol{s} = (p_x, p_y, 0)$ represents the position at the entrance pupil. With these definitions, the sagittal unit vector $\mathbf{e}_S$ at the mask, which is perpendicular to the outgoing momentum $\boldsymbol{p} + \boldsymbol{s}_0$ and the chief ray momentum $\boldsymbol{s}_0$ (both are in the meridional plane as shown in Fig. 8), is written as follows,

$$\mathbf{e}_S = \frac{(\boldsymbol{p} + \boldsymbol{s}_0) \times \boldsymbol{s}_0}{|(\boldsymbol{p} + \boldsymbol{s}_0) \times \boldsymbol{s}_0|} = \frac{\boldsymbol{p} \times \boldsymbol{s}_0}{|\boldsymbol{p} \times \boldsymbol{s}_0|}. \tag{28}$$

The meridional unit vector $\mathbf{e}_M$ at the mask is perpendicular to the sagittal unit vector $\mathbf{e}_S$ and the outgoing momentum $\boldsymbol{p} + \boldsymbol{s}_0$ as follows,

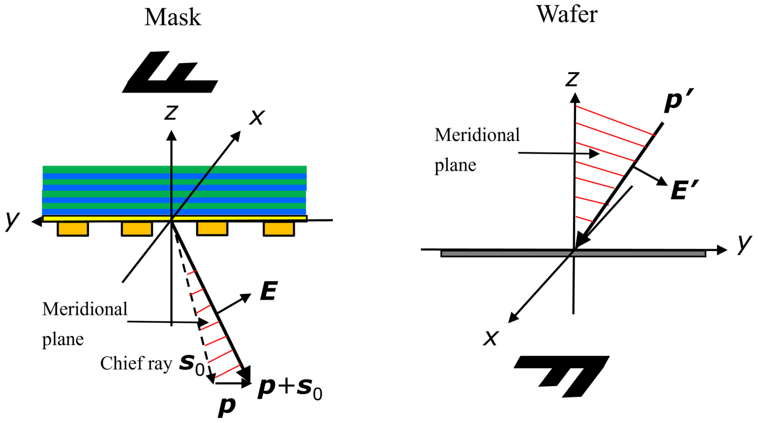

Fig. 8 Outgoing wave at the mask and incoming wave at the wafer.

$$\mathbf{e}_\mathrm{M} = \mathbf{e}_\mathrm{S} \times \frac{(\boldsymbol{p}+\boldsymbol{s}_0)}{|\boldsymbol{p}+\boldsymbol{s}_0|}. \tag{29}$$

The incoming momentum at the wafer $\boldsymbol{p}'$ is related to $\boldsymbol{p}$ by the following equation,

$$\boldsymbol{p}' = \left(M_x p_x, M_y p_y, -\sqrt{k^2 - (M_x p_x)^2 - (M_y p_y)^2}\right). \tag{30}$$

Then, the sagittal unit vector $\mathbf{e}'_S$ and the meridional unit vector $\mathbf{e}'_M$ at the wafer are written as follows (see Fig. 8),

$$\mathbf{e}'_S = \frac{\boldsymbol{p}' \times \mathbf{e}'_z}{|\boldsymbol{p}' \times \mathbf{e}'_z|}, \tag{31}$$

$$\mathbf{e}'_M = \mathbf{e}'_S \times \frac{\boldsymbol{p}'}{k}, \tag{32}$$

where $\mathbf{e}'_z = (0, 0, 1)$.

With these definitions, the electric field at the mask $\boldsymbol{E}$ and the electric field at the wafer $\boldsymbol{E}'$ are related by the following equation,

$$\boldsymbol{E}' = (\boldsymbol{E} \cdot \mathbf{e}_S)\mathbf{e}'_S + (\boldsymbol{E} \cdot \mathbf{e}_M)\mathbf{e}'_M. \tag{33}$$

Equation (33) is rewritten as a matrix equation as follows,

$$\boldsymbol{E}' = R\boldsymbol{E}, \tag{34}$$

where R is a rotation matrix defined by

$$R_{\alpha\beta}(\boldsymbol{p}) = e'_{S,\alpha}(\boldsymbol{p})e_{S,\beta}(\boldsymbol{p}) + e'_{M,\alpha}(\boldsymbol{p})e_{M,\beta}(\boldsymbol{p}) \;\; \alpha, \beta = x, y, z. \tag{35}$$

3.4 Coherence Function

The electric field rotates inside the projection optics from $\boldsymbol{E}$ to $\boldsymbol{E}' = R\boldsymbol{E}$. Then, according to Abbe's theory, the image intensity on the wafer is written as follows,

$$I_\rho(\boldsymbol{x}) = \iint S_\rho(\boldsymbol{s}) \left| \iint R(\boldsymbol{q}+\boldsymbol{s})\boldsymbol{E}_\rho(\boldsymbol{q};\boldsymbol{s})P(\boldsymbol{q}+\boldsymbol{s})e^{i(Mq_x x + M_y q_y y)}\mathrm{d}\boldsymbol{q} \right|^2 \mathrm{d}\boldsymbol{s}, \tag{36}$$

where ρ represents the polarization X or Y. We assume the linear polarization for the effective source S. The polarization of the effective source and that of the electric field in the projection optics are the same because the polarization changes at the mask are ignored, as discussed in Sec. 3.2.

In Sec. 2, we converted Eq. (6) to the STCC formula. If we straightforwardly use the same method to Eq. (36), *TCC*, *TCCSX* and *TCCSY* become 3×3 matrices due to the rotation matrix R. This can be avoided by changing the variable from the electric field to the vector potential. From Eq. (19), the electric field at the mask $\boldsymbol{E}_\rho$ is written in terms of the vector potential $\boldsymbol{A}_\rho$ as follows,

$$\boldsymbol{E}_\rho(\boldsymbol{q};\boldsymbol{s}) = ik\boldsymbol{A}_\rho(\boldsymbol{q};\boldsymbol{s}) - i\frac{\boldsymbol{k}\cdot\boldsymbol{A}_\rho(\boldsymbol{q};\boldsymbol{s})}{k}\boldsymbol{k}, \tag{37}$$

where

$$\boldsymbol{k} = k\frac{(\boldsymbol{p}+\boldsymbol{s}_0)}{|\boldsymbol{p}+\boldsymbol{s}_0|}. \tag{38}$$

As the unit vectors $\mathbf{e}_S$ and $\mathbf{e}_M$ are perpendicular to the momentum $\boldsymbol{p}+\boldsymbol{s}_0$,

$$\mathbf{e}_S\cdot\boldsymbol{k} = \mathbf{e}_M\cdot\boldsymbol{k} = 0. \tag{39}$$

Therefore,

$$R\boldsymbol{k} = 0, \tag{40}$$

and

$$R\boldsymbol{E}_\rho(\boldsymbol{q};\boldsymbol{s}) = ikR\boldsymbol{A}_\rho(\boldsymbol{q};\boldsymbol{s}). \tag{41}$$

This equation simplifies Eq. (36) and provides an advantage when converting Eq. (36) to the STCC formula because $\boldsymbol{A}_\rho(\boldsymbol{q};\boldsymbol{s})$ has only one component.

The vector potential $\boldsymbol{A}_\rho(\boldsymbol{q};\boldsymbol{s})$ is the amplitude of the outgoing wave from the mask as follows,

$$\boldsymbol{A}_X(\boldsymbol{q};\boldsymbol{s}) = \frac{1}{\sqrt{k^2-s_x^2}}(A_X^{\mathrm{rel}}(\boldsymbol{q};\boldsymbol{s}),0,0), \tag{42}$$

$$\boldsymbol{A}_Y(\boldsymbol{q};\boldsymbol{s}) = \frac{1}{\sqrt{k^2-s_y^2}}(0,A_Y^{\mathrm{rel}}(\boldsymbol{q};\boldsymbol{s}),0), \tag{43}$$

where $A_X^{\mathrm{rel}}(\boldsymbol{q};\boldsymbol{s})$ and $A_Y^{\mathrm{rel}}(\boldsymbol{q};\boldsymbol{s})$ are the relative amplitudes of the outgoing vector potentials from the mask, assuming the amplitudes of the vector potentials at the effective source are one. These values are calculated by the waveguide model.[11]

The factor $1\Big/\sqrt{k^2-s_\rho^2}$ is the normalization factor at the effective source explained below. At the effective source, the electric field $\boldsymbol{E}_\rho(\boldsymbol{s})$ and the vector potential $\boldsymbol{A}_\rho(\boldsymbol{s})$ are related by

$$\boldsymbol{E}_\rho(\boldsymbol{s}) = ik\boldsymbol{A}_\rho(\boldsymbol{s}) - i\frac{\mathbf{s}\cdot\boldsymbol{A}_\rho(\boldsymbol{s})}{k}\,\mathbf{s}. \tag{44}$$

The normalization factor is derived by assuming the strength of the electric field at each source point is one, a convention commonly used in lithography simulations,

$$|\boldsymbol{E}_\rho(\boldsymbol{s})|^2 = k^2|\boldsymbol{A}_\rho(\boldsymbol{s})|^2 - |\mathbf{s}\cdot\boldsymbol{A}_\rho(\boldsymbol{s})|^2 = (k^2-s_\rho^2)|\boldsymbol{A}_\rho(\boldsymbol{s})|^2 = 1. \tag{45}$$

Therefore, the normalization factor is $1/\sqrt{k^2-s_\rho^2}$. When there are N source points, the total image intensity will be divided by N after the simulation.

Inserting Eqs. (41)–(43) into Eq. (36) we obtain,

$$\begin{aligned} I_\rho(\boldsymbol{x}) = \iint & S_\rho(\boldsymbol{s})P(\boldsymbol{q}+\boldsymbol{s})P^*(\boldsymbol{q}'+\boldsymbol{s})C_\rho(\boldsymbol{q}'+\boldsymbol{s};\boldsymbol{q}+\ \boldsymbol{s}) \\ & \times\frac{k^2}{k^2-s_\rho^2}A_\rho^{\mathrm{rel}}(\boldsymbol{q};\boldsymbol{s})A_\rho^{\mathrm{rel}*}(\boldsymbol{q}';\boldsymbol{s})\mathrm{e}^{i(M_x(q_x-q_x')x+M_y(q_y-q_y')y)}\mathrm{d}\boldsymbol{s}\,\mathrm{d}\boldsymbol{q}\,\mathrm{d}\boldsymbol{q}', \end{aligned} \tag{46}$$

where C_ρ is a coherence function defined by

$$C_\rho(\boldsymbol{p}';\boldsymbol{p}) = (R^T(\boldsymbol{p}')R(\boldsymbol{p}))_{\rho\rho} = \mathbf{e}_S'(\boldsymbol{p}')\cdot\mathbf{e}_S'(\boldsymbol{p})\mathrm{e}_{S,\rho}(\boldsymbol{p}')\mathrm{e}_{S,\rho}(\boldsymbol{p}) + \mathbf{e}_M'(\boldsymbol{p}')\cdot\mathbf{e}_M'(\boldsymbol{p})e_{M,\rho}(\boldsymbol{p}')e_{M,\rho}(\boldsymbol{p}). \tag{47}$$

This function represents the coherent loss of two rays coming from different directions, which depends on the polarization ρ. Figure 9 shows examples of the coherence functions when the two rays come to the wafer from opposite directions, i.e., $\boldsymbol{p}'=-\boldsymbol{p}$. As shown in the figure, the values of the coherence functions become small (coherent losses become large) when the following two

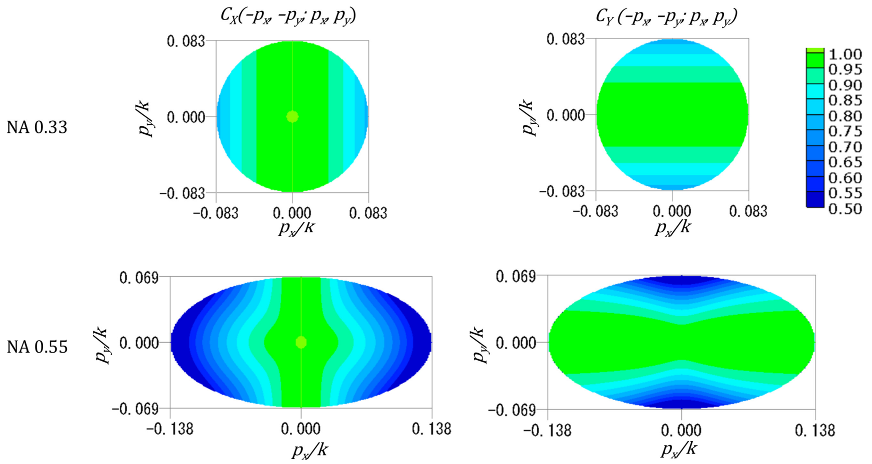

Fig. 9 Examples of coherence functions for NA 0.33 and NA 0.55.

conditions are satisfied: a) the direction of the incoming waves is parallel to the polarization (i.e., polarization in the meridional plane) and b) the incident angle (p_x or p_y) is large. This effect becomes large for high-NA optics.

So far, we have assumed that the effective source is linearly polarized in the X or Y direction. In general, the polarization of the effective source depends on the source position.[20] In this case, the diffraction amplitude from the EUV mask becomes the weighted sum of the two polarizations as follows:

$$\boldsymbol{E}(\boldsymbol{q};\boldsymbol{s}) = \sqrt{S_X(\boldsymbol{s})}\boldsymbol{E}_X(\boldsymbol{q};\boldsymbol{s}) + \sqrt{S_Y(\boldsymbol{s})}e^{i\phi(\boldsymbol{s})}\boldsymbol{E}_Y(\boldsymbol{q};\boldsymbol{s}), \tag{48}$$

where $\phi(\boldsymbol{s})$ is the phase delay between the X and Y polarizations. Then, Eq. (36) is rewritten as follows,

$$\begin{aligned} I(\boldsymbol{x}) &= \iint \left| \iint R(\boldsymbol{q}+\boldsymbol{s})\left\{\sqrt{S_X(\boldsymbol{s})}\boldsymbol{E}_X(\boldsymbol{q};\boldsymbol{s}) + \sqrt{S_Y(\boldsymbol{s})}e^{i\phi(\boldsymbol{s})}\boldsymbol{E}_Y(\boldsymbol{q};\boldsymbol{s})\right\} P(\boldsymbol{q}+\boldsymbol{s})e^{i(M_x q_x x + M_y q_y y)}\mathrm{d}\boldsymbol{q}\right|^2 \mathrm{d}\boldsymbol{s} \\ &= I_X(\boldsymbol{x}) + I_Y(\boldsymbol{x}) + 2\mathrm{Re}\left\{\iint \sqrt{S_X(\boldsymbol{s})S_Y(\boldsymbol{s})}e^{-i\phi(\boldsymbol{s})}P(\boldsymbol{q}+\boldsymbol{s})P^*(\boldsymbol{q}'+\boldsymbol{s})(R^{\mathrm{T}}(\boldsymbol{q}'+\boldsymbol{s})R(\boldsymbol{q}+\boldsymbol{s}))_{yx} \right. \\ &\quad \left. \times \frac{k^2}{\sqrt{(k^2-s_x^2)(k^2-s_y^2)}} A_X^{\mathrm{rel}}(\boldsymbol{q};\boldsymbol{s})A_Y^{\mathrm{rel}*}(\boldsymbol{q}';\boldsymbol{s})\mathrm{e}^{\mathrm{i}(M_x(q_x-q'_x)x + M_y(q_y-q'_y)y)}\mathrm{d}\boldsymbol{s}\,\mathrm{d}\boldsymbol{q}\,\mathrm{d}\boldsymbol{q}'\right\}. \end{aligned} \tag{49}$$

3.5 STCC Formula Including the Polarization Effect

The vector potential is expanded as a linear function of the source position, as shown in Eq. (7), as follows,

$$A_\rho^{\mathrm{rel}}(\boldsymbol{q};\boldsymbol{s}) \cong A_\rho(\boldsymbol{q}) + \partial_{s_x}A_\rho(\boldsymbol{q})(s_x + q_x/2) + \partial_{s_y}A_\rho(\boldsymbol{q})(s_y + q_y/2), \tag{50}$$

where

$$A_\rho(\boldsymbol{q}) = A_\rho^{\mathrm{rel}}(\boldsymbol{q};\boldsymbol{s} = -\boldsymbol{q}/2), \tag{51}$$

$$\partial_{s_x}A_\rho(\boldsymbol{q}) = \left.\frac{\partial A_\rho^{\mathrm{rel}}(\boldsymbol{q};\boldsymbol{s})}{\partial s_x}\right|_{\boldsymbol{s}=-\boldsymbol{q}/2}, \tag{52}$$

$$\partial_{s_y}A_\rho(\boldsymbol{q}) = \left.\frac{\partial A_\rho^{\mathrm{rel}}(\boldsymbol{q};\boldsymbol{s})}{\partial s_y}\right|_{\boldsymbol{s}=-\boldsymbol{q}/2}. \tag{53}$$

Inserting Eq. (50) into Eq. (46) and neglecting the second-order terms of s_x and s_y, we obtain,

$$\begin{aligned} I_\rho(\boldsymbol{x}) \cong & \iint TCC_\rho(\boldsymbol{q};\boldsymbol{q}')A_\rho(\boldsymbol{q})A_\rho^*(\boldsymbol{q}')\mathrm{e}^{i(M_x(q_x-q_x')x+M_y(q_y-q_y')y)}\mathrm{d}\boldsymbol{q}\,\mathrm{d}\boldsymbol{q}' \\ & +2\,\mathrm{Re}\left\{\iint TCC_\rho(\boldsymbol{q};\boldsymbol{q}')A_\rho(\boldsymbol{q})\left(\partial_{s_x}A_\rho^*(\boldsymbol{q}')\frac{q_x'}{2}+\partial_{s_y}A_\rho^*(\boldsymbol{q}')\frac{q_y'}{2}\right)\mathrm{e}^{i(M_x(q_x-q_x')x+M_y(q_y-q_y')y)}\mathrm{d}\boldsymbol{q}\,\mathrm{d}\boldsymbol{q}'\right\} \\ & +2\,\mathrm{Re}\left\{\iint TCCSX_\rho(\boldsymbol{q};\boldsymbol{q}')A_\rho(\boldsymbol{q})\partial_{s_x}A_\rho^*(\boldsymbol{q}')\mathrm{e}^{i(M_x(q_x-q_x')x+M_y(q_y-q_y')y)}\mathrm{d}\boldsymbol{q}\,\mathrm{d}\boldsymbol{q}'\right\} \\ & +2\,\mathrm{Re}\left\{\iint TCCSY_\rho(\boldsymbol{q};\boldsymbol{q}')A_\rho(\boldsymbol{q})\partial_{s_y}A_\rho^*(\boldsymbol{q}')\mathrm{e}^{i(M_x(q_x-q_x')x+M_y(q_y-q_y')y)}\mathrm{d}\boldsymbol{q}\,\mathrm{d}\boldsymbol{q}'\right\} \end{aligned} \tag{54}$$

where

$$TCC_\rho(\boldsymbol{q};\boldsymbol{q}') = \iint S_\rho(\boldsymbol{s})P(\boldsymbol{q}+\boldsymbol{s})P^*(\boldsymbol{q}'+\boldsymbol{s})C_\rho(\boldsymbol{q}'+\boldsymbol{s};\boldsymbol{q}+\boldsymbol{s})\frac{k^2}{k^2-s_\rho^2}\mathrm{d}\boldsymbol{s}, \tag{55}$$

$$TCCSX_\rho(\boldsymbol{q};\boldsymbol{q}') = \iint s_x S_\rho(\boldsymbol{s})P(\boldsymbol{q}+\boldsymbol{s})P^*(\boldsymbol{q}'+\boldsymbol{s})C_\rho(\boldsymbol{q}'+\boldsymbol{s};\boldsymbol{q}+\boldsymbol{s})\frac{k^2}{k^2-s_\rho^2}\mathrm{d}\boldsymbol{s}, \tag{56}$$

$$TCCSY_\rho(\boldsymbol{q};\boldsymbol{q}') = \iint s_y S_\rho(\boldsymbol{s})P(\boldsymbol{q}+\boldsymbol{s})P^*(\boldsymbol{q}'+\boldsymbol{s})C_\rho(\boldsymbol{q}'+\boldsymbol{s};\boldsymbol{q}+\boldsymbol{s})\frac{k^2}{k^2-s_\rho^2}\mathrm{d}\boldsymbol{s}. \tag{57}$$

Equations (54)–(57) represent the STCC formula including the polarization effect. The coherence function C_ρ, which reflects the rotation of the electric field, is introduced into TCCs. The number of TCCs is doubled to six from the STCC formula in Sec. 2 without the polarization effect. As the six TCCs are Hermitian matrices, the SOCS model can be applied to Eqs. (55)–(57) in the same way as Eqs. (16)–(18).

Figure 10 shows the polarization dependence of the image intensities for NA 0.33 and NA 0.55. STCC formula, Eq. (54) was used for calculations. The mask pattern and the optical setting for NA 0.33 are the same as in Fig. 3. For NA 0.55, the mask pattern has 9 nm horizontal spaces, and the illumination setting is the dipole illumination DY90 with $\sigma_{\text{in}}/\sigma_{\text{out}} = 0.55/0.9$. As shown in Fig. 10, the polarization effect for NA 0.55 is much larger than that for NA 0.33.

4 Accuracy of the STCC Formula

In this section, the accuracy of the STCC formula is studied using several test patterns. Figures 11–13 show the results for NA 0.33. The simple threshold model is used to calculate CDs. The polarization is X polarization. Although it is not shown in the figures, similar results were obtained for Y polarization.

In the figures, EM represents the electromagnetic simulation[11] using Abbe's theory, Eq. (36). FT represents the thin mask model using the Fourier transformation of the mask pattern. The

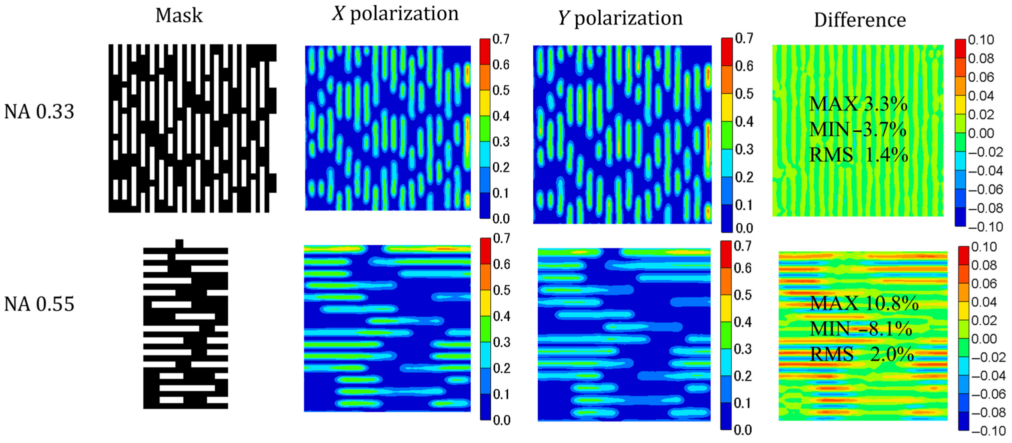

Fig. 10 Polarization dependence of the image intensities for NA 0.33 and NA 0.55.

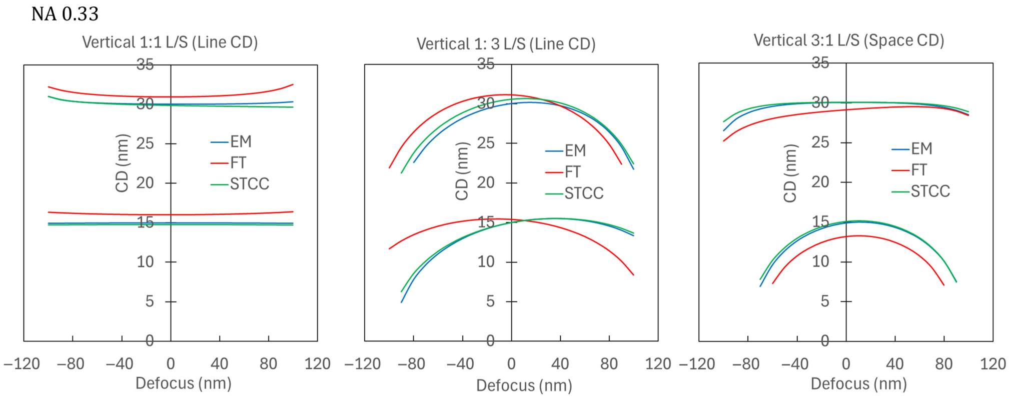

Fig. 11 CD-focus curves of vertical L/S with several pitches and line (or space) widths. The optical setting is NA 0.33, and the dipole illumination is DX90 with $\sigma_{\text{in}}/\sigma_{\text{out}} = 0.55/0.9$.

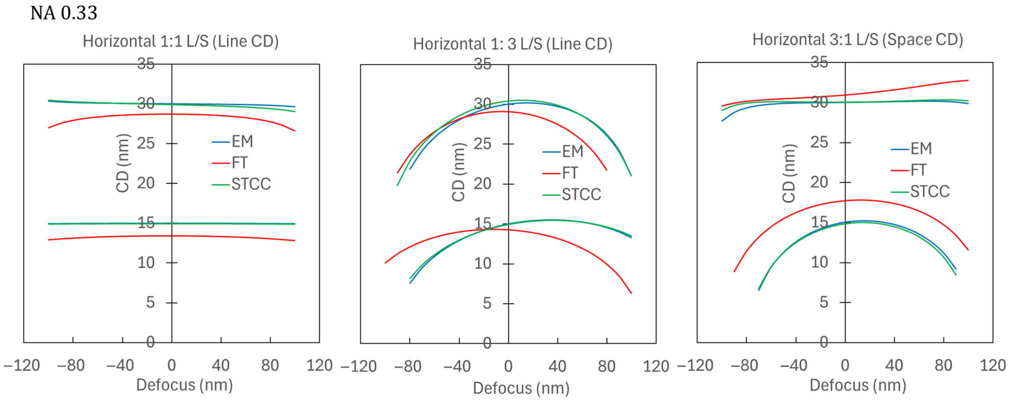

Fig. 12 CD-focus curves of horizontal L/S with several pitches and line (or space) widths. The optical setting is NA 0.33, and the dipole illumination is DY90 with $\sigma_{\text{in}}/\sigma_{\text{out}} = 0.55/0.9$.

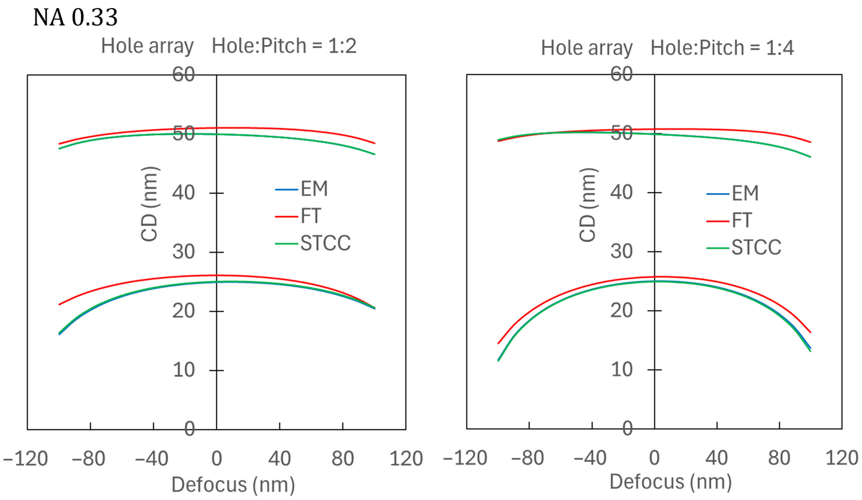

Fig. 13 CD-focus curves of hole arrays with several pitches and hole sizes. The optical setting is NA 0.33, and the annular illumination with $\sigma_{\text{in}}/\sigma_{\text{out}} = 0.6/0.85$.

M3D parameters used in the STCC formula are calculated by the least square fitting to the EM amplitudes. As shown in the figures, the agreement between the EM simulation and the STCC formula is very good.

Figures 14–16 show the results for NA 0.55. The agreement between the EM simulation and the STCC formula is good for horizontal L/S and hole patterns. However, there are some discrepancies in the vertical L/S, especially the 1:1 L/S.

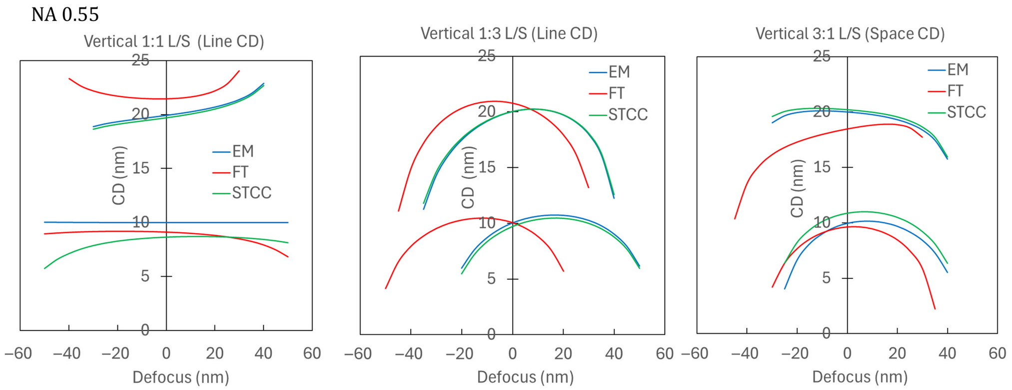

Fig. 14 CD-focus curves of vertical L/S with several pitches and line (or space) widths. The optical setting is NA 0.55, and the dipole illumination is DX90 with $\sigma_{\text{in}}/\sigma_{\text{out}} = 0.55/0.9$.

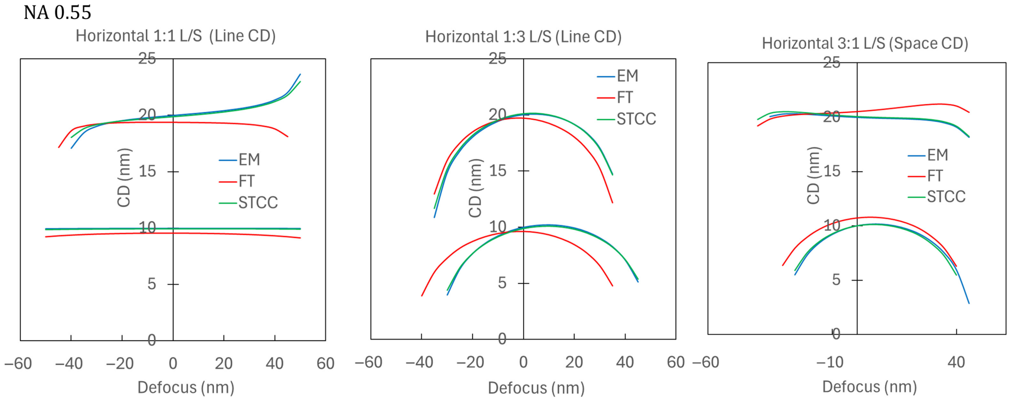

Fig. 15 CD-focus curves of horizontal L/S with several pitches and line (or space) widths. The optical setting is NA 0.55, and the dipole illumination is DY90 with $\sigma_{\text{in}}/\sigma_{\text{out}} = 0.55/0.9$.

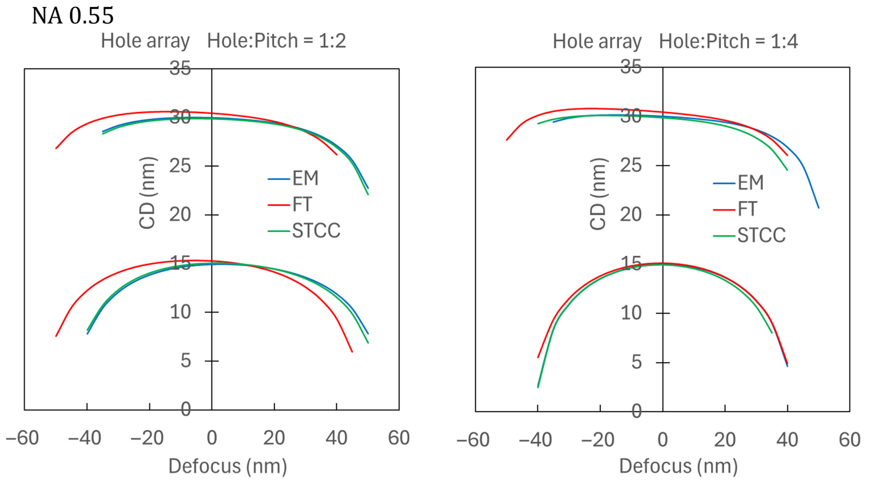

Fig. 16 CD-focus curves of hole arrays with several pitches and hole sizes. The optical setting is NA 0.55, and the annular illumination with $\sigma_{\text{in}}/\sigma_{\text{out}} = 0.6/0.85$.

The root cause of the discrepancies was found to be the linear approximation of the diffraction amplitude in the STCC formula. Figure 17 compares the source position dependence of the 0th order diffraction amplitude, $\text{Real}(A_x^{\text{3D}}(0,0;s_x,s_y))$, for vertical and horizontal L/S for NA 0.33 and NA 0.55. The diffraction amplitude of the horizontal L/S depends mainly on the y direction. As the chief ray at the mask is tilted in the y direction, the source position dependence (deviation from the chief ray) of the amplitude can be approximated by a linear function. On the other hand, the diffraction amplitude of the vertical L/S depends mainly on the x direction. At the

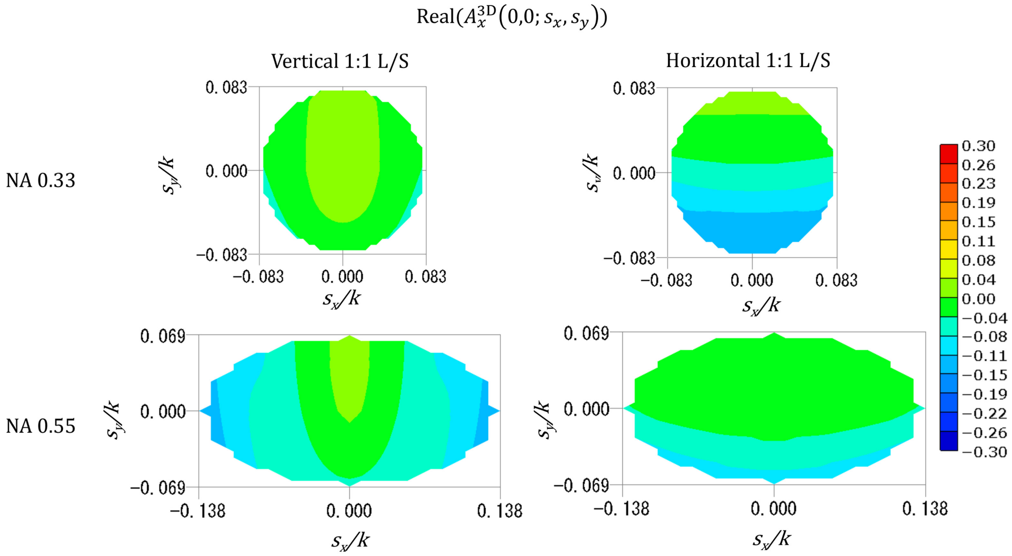

Fig. 17 Source position dependence of the 0th order diffraction amplitudes for vertical and horizontal L/S for NA 0.33 and NA 0.55.

center of the illumination slit where the azimuthal angle is zero, the source position dependence of the diffraction amplitude in the x direction is quadratic. This effect becomes large for NA 0.55 because the maximum incident angle in the x direction is large. The STCC formula in Sec. 4 ignores the quadratic terms. For NA 0.55, when the mask pattern contains vertical lines, the STCC formula needs to be extended to include a quadratic term in the x direction.

The linear expansion of the vector potential in Eq. (50) is extended by including the quadratic term in the x direction as follows,

$$A_\rho^{\mathrm{rel}}(\boldsymbol{q};\boldsymbol{s}) \cong A_\rho(\boldsymbol{q}) + \partial_{s_x} A_\rho(\boldsymbol{q}) s_x + \partial_{s_x}^2 A_\rho(\boldsymbol{q}) s_x^2 + \partial_{s_y} A_\rho(\boldsymbol{q}) s_y. \tag{58}$$

The origin of the expansion is $\boldsymbol{s} = \boldsymbol{0}$. In Eq. (54), we set the origin of the expansion at $\boldsymbol{s} = -\boldsymbol{q}/2$ and ignored the second-order terms of s_x and s_y. However, when the quadratic term is added, it is better to set the origin at $\boldsymbol{s} = \boldsymbol{0}$ and calculate all terms. Then, the STCC formula is written as follows:

$$\begin{aligned}
I_\rho(\boldsymbol{x}) \cong & \iint TCC_\rho(\boldsymbol{q};\boldsymbol{q}')A_\rho(\boldsymbol{q})A_\rho^*(\boldsymbol{q}')\mathrm{e}^{i(M_x(q_x-q_x')x+M_y(q_y-q_y')y)}\mathrm{d}\boldsymbol{q}\,\mathrm{d}\boldsymbol{q}' \\
& + \iint TCCSX2Y0_\rho(\boldsymbol{q};\boldsymbol{q}')\partial_{s_x}A_\rho(\boldsymbol{q})\partial_{s_x}A_\rho^*(\boldsymbol{q}')\mathrm{e}^{i(M_x(q_x-q_x')x+M_y(q_y-q_y')y)}\mathrm{d}\boldsymbol{q}\,\mathrm{d}\boldsymbol{q}' \\
& + \iint TCCSX4Y0_\rho(\boldsymbol{q};\boldsymbol{q}')\partial_{s_x}^2A_\rho(\boldsymbol{q})\partial_{s_x}^2A_\rho^*(\boldsymbol{q}')\mathrm{e}^{i(M_x(q_x-q_x')x+M_y(q_y-q_y')y)}\mathrm{d}\boldsymbol{q}\,\mathrm{d}\boldsymbol{q}' \\
& + \iint TCCSX0Y2_\rho(\boldsymbol{q};\boldsymbol{q}')\partial_{s_y}A_\rho(\boldsymbol{q})\partial_{s_y}A_\rho^*(\boldsymbol{q}')\mathrm{e}^{i(M_x(q_x-q_x')x+M_y(q_y-q_y')y)}\mathrm{d}\boldsymbol{q}\,\mathrm{d}\boldsymbol{q} \\
& + 2\,\mathrm{Re}\left\{\iint TCCSX1Y0_\rho(\boldsymbol{q};\boldsymbol{q}')A_\rho(\boldsymbol{q})\partial_{s_x}A_\rho^*(\boldsymbol{q}')\ \mathrm{e}^{i(M_x(q_x-q_x')x+M_y(q_y-q_y')y)}\mathrm{d}\boldsymbol{q}\,\mathrm{d}\boldsymbol{q}'\right\} \\
& + 2\,\mathrm{Re}\left\{\iint TCCSX2Y0_\rho(\boldsymbol{q};\boldsymbol{q}')A_\rho(\boldsymbol{q})\partial_{s_x}^2A_\rho^*(\boldsymbol{q}')\mathrm{e}^{i(M_x(q_x-q_x')x+M_y(q_y-q_y')y)}\mathrm{d}\boldsymbol{q}\,\mathrm{d}\boldsymbol{q}'\right\} \\
& + 2\,\mathrm{Re}\left\{\iint TCCSX0Y1_\rho(\boldsymbol{q};\boldsymbol{q}')A_\rho(\boldsymbol{q})\partial_{s_y}A_\rho^*(\boldsymbol{q}')\mathrm{e}^{i(M_x(q_x-q_x')x+M_y(q_y-q_y')y)}\mathrm{d}\boldsymbol{q}\,\mathrm{d}\boldsymbol{q}'\right\} \\
& + 2\,\mathrm{Re}\left\{\iint TCCSX3Y0_\rho(\boldsymbol{q};\boldsymbol{q}')\partial_{s_x}A_\rho(\boldsymbol{q})\partial_{s_x}^2A_\rho^*(\boldsymbol{q}')\mathrm{e}^{i(M_x(q_x-q_x')x+M_y(q_y-q_y')y)}\mathrm{d}\boldsymbol{q}\,\mathrm{d}\boldsymbol{q}'\right\} \\
& + 2\,\mathrm{Re}\left\{\iint TCCSX1Y1_\rho(\boldsymbol{q};\boldsymbol{q}')\partial_{s_x}A_\rho(\boldsymbol{q})\partial_{s_y}A_\rho^*(\boldsymbol{q}')\mathrm{e}^{i(M_x(q_x-q_x')x+M_y(q_y-q_y')y)}\mathrm{d}\boldsymbol{q}\,\mathrm{d}\boldsymbol{q}'\right\} \\
& + 2\,\mathrm{Re}\left\{\iint TCCSX2Y1_\rho(\boldsymbol{q};\boldsymbol{q}')\partial_{s_x}^2A_\rho(\boldsymbol{q})\partial_{s_y}A_\rho^*(\boldsymbol{q}')\mathrm{e}^{i(M_x(q_x-q_x')x+M_y(q_y-q_y')y)}\mathrm{d}\boldsymbol{q}\,\mathrm{d}\boldsymbol{q}'\right\},
\end{aligned} \tag{59}$$

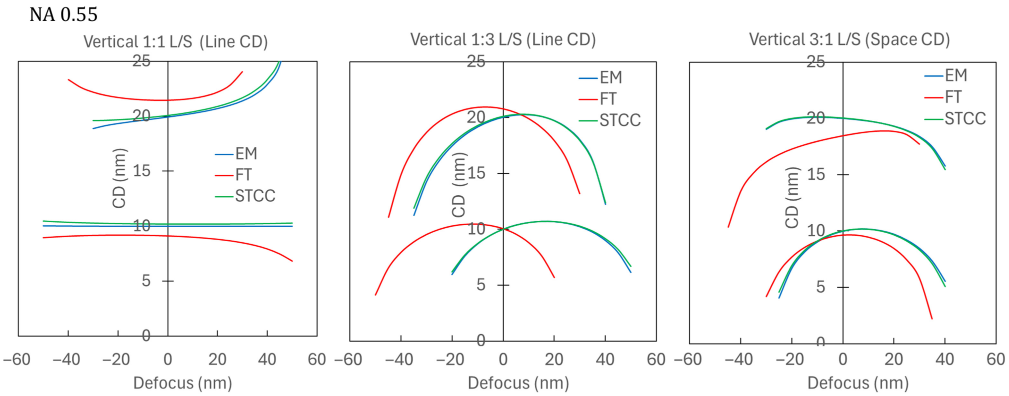

Fig. 18 CD-focus curves of vertical L/S with several pitches and line (or space) widths. The quadratic term is included in the STCC formula. The optical setting is NA 0.55, and the dipole illumination is DX90 with $\sigma_{\mathrm{in}}/\sigma_{\mathrm{out}} = 0.55/0.9$.

where

$$TCCSXiYj_\rho(\boldsymbol{q};\boldsymbol{q}') = \iint s_x^i s_y^j S_\rho(\boldsymbol{s}) P(\boldsymbol{q}+\boldsymbol{s}) P^*(\boldsymbol{q}+\boldsymbol{s}) C_\rho(\boldsymbol{q}+\boldsymbol{s};\boldsymbol{q}+\boldsymbol{s}) \frac{k^2}{k^2 - s_\rho^2} \mathrm{d}\boldsymbol{s}. \tag{60}$$

In total, 18 TCCs appear in Eq. (59). Figure 18 shows the results of the calculations using the STCC formula in Eq. (59). The agreement between the EM simulation and the STCC formula becomes much better than the results in Fig. 14.

5 CNN Model for Fast EUV Lithography Simulation

In this section, we provide an overview of our CNN model for fast EUV lithography simulation. This model can be applied to high-NA lithography simulations. Details of the model are given in Ref. 11. The diffraction amplitudes from an EUV mask can be calculated rigorously by the EM simulation. However, the EM simulation is highly time-consuming and not suited for OPC applications. Our CNN model reproduces the results of EM simulations quickly.

The diffraction momentum $\boldsymbol{q}$ is discretized assuming a periodic mask pattern. When a mask pattern has period L (wafer scale) in the x and y directions, the diffraction momentum from the mask is discretized as follows,

$$(q_x, q_y) = \left(\frac{2\pi l}{LM_x}, \frac{2\pi m}{LM_y}\right), \tag{61}$$

where l and m are diffraction orders (integers) in the x and y directions. In the 3D waveguide model,[11] the source position $\boldsymbol{s}$ is also discretized as follows,

$$(s_x, s_y) = \left(\frac{2\pi l_s}{LM_x}, \frac{2\pi m_s}{LM_y}\right), \tag{62}$$

where l_s and m_s are integers. Then, the diffraction amplitude of the outgoing wave $A_\rho(l, m; l_s, m_s) \equiv A_\rho^{\mathrm{rel}}(q_x, q_y; s_x, s_y)$ depends on the diffraction order (l, m) and the source position (l_s, m_s). The diffraction amplitude is divided into the thin mask amplitude and the M3D amplitude as follows.

$$A_\rho(l, m; l_s, m_s) = A_\rho^{\mathrm{FT}}(l, m) + A_\rho^{\mathrm{3D}}(l, m; l_s, m_s). \tag{63}$$

The thin mask amplitude $A_\rho^{\mathrm{FT}}(l, m)$ is calculated from the Fourier transform of the mask pattern, and it does not depend on the source position (l_s, m_s). On the other hand, the M3D amplitude $A_\rho^{\mathrm{3D}}(l, m; l_s, m_s)$ depends on the source position (l_s, m_s).

Figure 19 shows an example of the diffraction amplitude calculated by the 3D waveguide model. The source position and the diffraction order are restricted by the source shape and the pupil shape as follows (see Fig. 2).

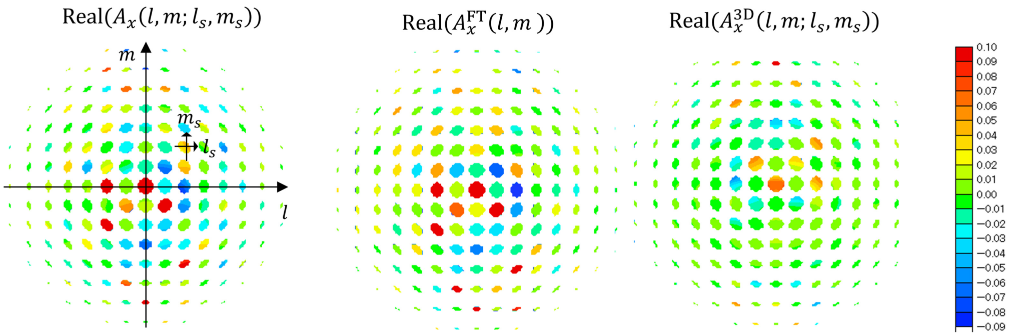

Fig. 19 Decomposition of the diffraction amplitude.

$$\sqrt{l_s^2+m_s^2} \le \mathrm{NA}\frac{L}{\lambda}, \tag{64}$$

$$\sqrt{(l+l_s)^2+(m+m_s)^2} \le \mathrm{NA}\frac{L}{\lambda}. \tag{65}$$

The contribution of the thin mask amplitude $A_x^{\mathrm{FT}}(l,m)$ is dominant. The M3D amplitude $A_\rho^{\mathrm{3D}}(l,m;l_s,m_s)$ smoothly depends on the source position (l_s,m_s), which is the basis of the STCC formula.

We approximate the M3D amplitude by a linear function of source position as follows,

$$A_\rho^{\mathrm{3D}}(l,m;l_s,m_s) \cong a_{\rho,0}(l,m) + a_{\rho,x}(l,m)(l_s+l/2) + a_{\rho,y}(l,m)(m_s+m/2), \tag{66}$$

where $a_{\rho,0}(l,m)$ is the average of the amplitudes in the overlapping area (Fig. 2), and $a_{\rho,x}(l,m)$ and $a_{\rho,y}(l,m)$ are the slopes of the amplitudes in x and y directions, respectively. We call these three numbers M3D parameters. These values are calculated by Eqs. (51)–(53). The M3D parameters represent the M3D effects of an EUV mask. They are determined by the mask pattern, absorber film structure, multilayer film structure, incident angle, and azimuthal angle. However, they do not depend on the source shape and the aberration of the pupil, including defocus.

Figure 20 shows a CNN in Ref. 11 that predicts M3D parameters. The input mask pattern has 2048 × 2048 binary data. We first convert them to 512 × 512 grayscale numbers by averaging the data. This is the input to CNN. Inside CNN, we repeat convolution, max pooling, and batch normalization five times. After flattening, two dense layers are added before the output.

The inference by CNN was 2400 times faster than the EM simulation. The inference time for M3D parameters was 0.05 s, excluding the time for the loading of the trained models. The time for image intensity integration by the STCC formula was 0.07 s. The total time was 0.12 s. The running time of CNN may not be fast enough for practical applications of OPC because it

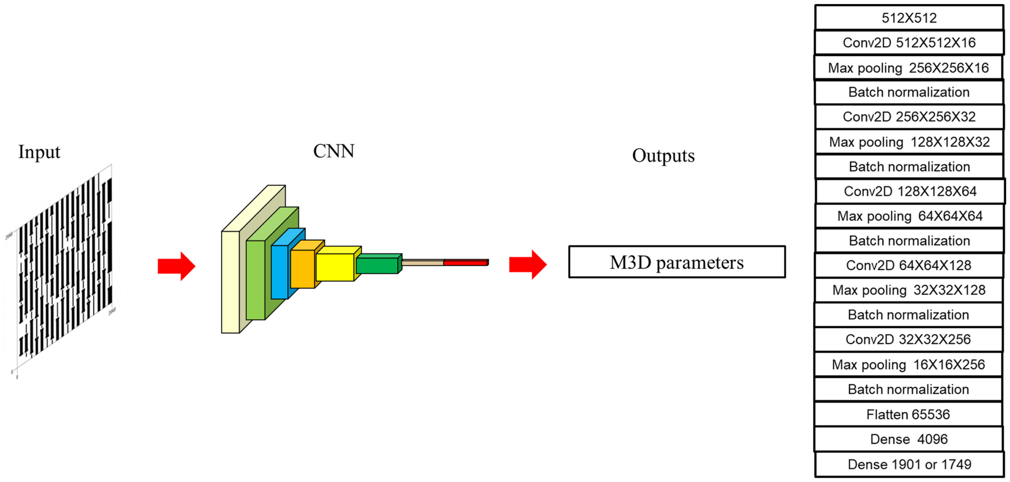

Fig. 20 CNN model predicting M3D parameters from an input mask pattern.

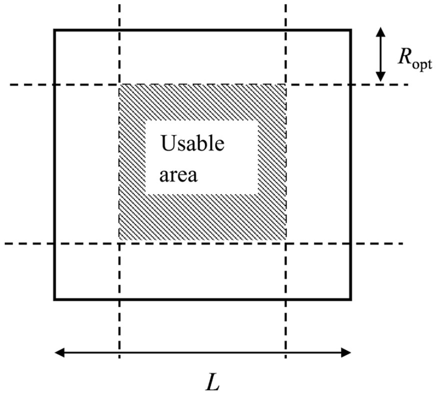

Fig. 21 Usable area and edge exclusion regions.

requires multiple iterations of image intensity calculations before converging. In this case, we might skip CNN calculations in the intermediate steps because the diffraction amplitude is dominated by the thin mask amplitude, which can be calculated by the Fourier transformation of the mask pattern.

The training mask patterns in Ref. 11 were Manhattan patterns. The remaining issue is how to build a CNN that can be applied to general mask patterns such as curvilinear patterns. We discuss this issue in a separate report.[21]

It is not explicitly stated in Eq. (66), but the M3D parameters depend on the azimuthal angle φ, which varies with the position of the illumination slit. Several CNNs at different slit positions are required to reproduce the slit position dependence of the M3D parameter.

As shown in Eqs. (64) and (65), the number of (l, m) pairs depends on the periodic length, L. Usually, the mask pattern of a product is not periodic. The edges of the mask pattern need to be excluded after the simulation to avoid the influence of the neighboring patterns (Fig. 21). The length of the exclusion region is estimated by the optical interaction range R_{opt} defined by[9]

$$R_{\text{opt}} = \frac{1.12\lambda}{\sigma \text{NA}}. \tag{67}$$

When NA = 0.33 and $\sigma = 0.5$, $R_{\text{opt}} = 92$ nm. The periodic length L must be larger than $2 \times R_{\text{opt}}$. This is the reason we set $L = 512$ nm. The exclusion region becomes larger when the illumination is more coherent, but it becomes smaller when the NA is larger.

6 Summary

The polarization effect depends on NA. The polarization effect for NA 0.55 is larger than that for NA 0.33. When the electric field is in the meridional plane, the image contrast is low in high-NA optics.

The STCC formula is extended to include the polarization effect. An additional coherence function C_ρ must be introduced into the STCC formula. C_ρ represents the effect of the electric field rotation in the meridional plane, which depends on the polarization $\rho = x$ or y. As a result, six TCCs (TCC_ρ, TCCSX_ρ, and TCCSY_ρ) are required to include the polarization effects in the STCC formula. For mask patterns including vertical lines, 18 TCCs are required.

The STCC formula expands the vector potential as a linear function of the source position. The coefficients of the linear function are named as M3D parameters. The CNN model infers M3D parameters from an input mask pattern. The inference by CNN is 2400 times faster than the EM simulation.

This work is based on the paper presented at SPIE Advanced Lithography + Patterning 2026.[22]

Disclosures

The authors declare there are no financial interests, commercial affiliations, or other potential conflicts of interest that have influenced the objectivity of this research or the writing of this paper.

Code and Data Availability

The code is available at https://github.com/takahashi-edalab/EUVlitho. All the data can be shared by the authors upon reasonable request.

Acknowledgments

This work was carried out using the TSUBAME4.0 supercomputer at Institute of Science Tokyo. This work was partially supported by JSPS KAKENHI Grant No. JP25K03090, MEXT Initiative to Establish Next-generation Novel Integrated Circuits Centers (X-NICS) Grant No. JPJ011438, and Japan Science and Technology Agency (JST) as part of Adopting Sustainable Partnerships for Innovative Research Ecosystem (ASPIRE), Grant No. JPMJAP2514.

References

1. V. Philipsen, "Mask is key to unlock full EUV potential," *Proc. SPIE* **11609**, 1160904 (2021).
2. A. Erdmann et al., "3D mask effects in high NA EUV imaging," *Proc. SPIE* **10957**, 109570Z (2019).
3. A. Wong and A. Neureuther, "Mask topography effects in projection printing of phase-shifting masks," *IEEE Trans. Electron Devices* **41**, 895 (1994).
4. M. G. Moharam and T. K. Gaylord, "Rigorous coupled-wave analysis of planar-grating diffraction," *J. Opt. Soc. Am.* **71**, 811 (1981).
5. K. D. Lucas, H. Tanabe, and A. J. Strojwas, "Efficient and rigorous three-dimensional model for optical lithography simulation," *J. Opt. Soc. Am. A* **13**, 2187 (1996).
6. N. B. Cobb, "Fast optical and process proximity correction algorithms for integrated circuit manufacturing," PhD dissertation, University of California, Berkeley (1998).
7. H. H. Hopkins, "On the diffraction theory of optical images," *Proc. R. Soc. Lond. A* **217**, 408 (1953).
8. M. Born and E. Wolf, *Principles of Optics*, 7th ed., Cambridge University Press (1999).
9. A. Wong, *Resolution Enhancement Techniques in Optical Lithography*, SPIE Press (2001).
10. H. Tanabe, A. Jinguji, and A. Takahashi, "Accelerating extreme ultraviolet lithography simulation with weakly guiding approximation and source position dependent transmission cross coefficient formula," *J. Micro/Nanopattern. Mater. Metrol.* **23**, 014201 (2024).
11. H. Tanabe, M. Shimoda, and A. Takahashi, "Rigorous electromagnetic simulator for extreme ultraviolet lithography and convolutional neural network reproducing electromagnetic simulations," *J. Micro/Nanopattern. Mater. Metrol.* **24**, 024201 (2025).
12. J. G. Santaclara et al., "The next step in Moore's law: high-NA EUV introduction at the customer," *Proc. SPIE* **12953**, 129530P (2024).
13. M. S. Yeung, "Modeling high numerical aperture optical lithography," *Proc. SPIE* **922**, 149 (1988).
14. D. G. Flagello, T. Milster, and A. E. Rosenbluth, "Theory of high-NA imaging in homogeneous thin films," *J. Opt. Soc. Am. A* **13**, 53 (1996).
15. H. Tanabe, A. Jinguji, and A. Takahashi, "Weakly guiding approximation of three-dimensional waveguide model for extreme ultraviolet lithography simulation," *J. Opt. Soc. Am. A* **41**, 1491 (2024).
16. D. Gloge, "Weakly guiding fibers," *Appl. Opt.* **10**, 2252 (1971).
17. S. Lin et al., "EUV APSM mask prospects and challenges," *Proc. SPIE* **12751**, 127510N (2023).
18. H. Kishida et al., "Development of cap layer for 1.Xnm node EUV blank," *Proc. SPIE* **13979**, 139791B (2026).
19. B. Richards and E. Wolf, "Electromagnetic diffraction in optical systems. II. Structure of the image field in an aplanatic system," *Proc. R. Soc. Lond. A* **253**, 358 (1959).
20. Y.-J. Chae et al., "Pixelated source polarization optimization for hyper-NA EUV lithography," *Proc. SPIE* **13686**, 136861F (2025).
21. M. Sugiyama, M. Shimoda, H. Tanabe, and A. Takahashi, "EUV M3D parameter prediction of curvilinear mask patterns by convolutional neural networks," *Proc. SPIE* **13980**, 139801J (2026).
22. H. Tanabe et al., "STCC formula including polarization and M3D effects in high-NA EUV lithography," *Proc. SPIE* **13979**, 139790G (2026).

Hiroyoshi Tanabe is a researcher at the Institute of Science Tokyo. He received his PhD degree in physics from the University of Tokyo in 1986. He has more than 35 years of experience in optical and EUV lithography. He is the author of more than 40 papers. He was the program committee chair of Photomask Japan in 2003 and 2004. His current research interests include EUV masks and lithography simulation. He is a member of SPIE.

Moe Sugiyama is currently a master's student at the Institute of Science Tokyo. The research focuses on machine learning and lithography simulation, particularly in the context of semiconductor process optimization.

Masayuki Shimoda received the BE, ME, and DE degrees in engineering from the Institute of Science Tokyo (formerly, Tokyo Institute of Technology), Tokyo, Japan, in 2018, 2020, and 2024, respectively. He is currently an assistant professor with the Department of Information and Communications Engineering of Institute of Science Tokyo. His current research interests include machine learning and VLSI physical design.

Atsushi Takahashi received his BE, ME, and DE degrees in electrical and electronic engineering from Tokyo Institute of Technology, Tokyo, Japan, in 1989, 1991, and 1996, respectively. He is currently a professor with the Department of Information and Communications Engineering, School of Engineering, Institute of Science Tokyo. His research interests are in VLSI layout design and combinational algorithms. He is a fellow of IEICE, a senior member of IEEE and IPSJ, and a member of ACM.